Cement and Concrete Composites 157 (2025) 105853

Contents lists available at ScienceDirect

Cement and Concrete Composites

journal homepage: www.elsevier.com/locate/cemconcomp

Minimizing the carbon footprint of 3D printing concrete: Leveraging parametric LCA and neural networks through multiobjective optimization

Willy Jin [a,b,*], Jean-François Caron [a], Claudiane M. Ouellet-Plamondon [b]

[a] Navier Laboratory, École des Ponts ParisTech, Gustave Eiffel University, CNRS, Champ-sur-Marne, France
[b] Department of Construction Engineering, École de Technologie Supérieure, Université du Québec, Montreal, Quebec, Canada

ARTICLE INFO

Keywords:
Limestone calcined clay
Life cycle assessment
3D printing
Optimization
Neural networks

ABSTRACT

Concrete 3D printing proposes an off-site industrial process allowing to deposit material only where required. However, most mixture design methods struggle to perform, which is why a majority of 3D printing materials display high clinker contents. This study proposes a reproducible methodology for tailor-made 3D printing materials. Applied to a low-clinker quaternary blend, an iterative optimization process leads to a significant reduction of labor in material tuning. It involves life cycle assessment and artificial neural networks as objective functions in the Pareto selection of best-performing solutions. Following the constitution of an 18-mixture database with 6 independent variables and 5 objective functions, printable mortars of different strength classes are designed within 2 to 4 active learning runs. Consequently, this optimum-driven technique allows to rapidly converge toward low-carbon solutions for 3D printing, using local materials and custom characterization procedures.

Introduction

The evolution of construction processes is moving toward solutions with reduced environmental impacts. 3D printing concrete (3DPC) proposes a way to avoid formwork manufacturing and reduce concrete volumes. However, the clinker proportion of 3D printing materials is generally 40% higher than conventional concretes [1–4], offsetting the material saving benefits with high carbon intensity. Concrete is a heterogeneous composite material with non-linear behavior [5], which depends on the proportions of each constituent, but also on their types and chemical compositions, as well as experimental conditions. This renders the tuning of fresh state properties for 3D printing demanding in time and resources, even more so in the context of one-component 3D printing (without accelerating admixture) as conflicting requirements must be fulfilled in the same timeframe [6]. On the other hand, specifications in the hardened state are equally important as they define the application and the use phase in the structure's life cycle. The optimal compromise between all these fresh and hardened properties is challenging to reach with a limited number of experimental runs and varying raw materials. Consequently, fresh state properties (pumpability, extrudability, buildability) are often prioritized over hardened state features (strength, durability) which are observed a posteriori [2]. **As a consequence, if it is considered, the minimization of environmental impacts is often a minor objective, leading to materials having higher cement proportions than necessary.**

Meanwhile, more than 80% of the impacts [7] originates from the material in the construction process, emphasizing the need for an efficient mix design process centered around the environmental impact. In this context, the development of alternative cementitious materials is active [8] and focused on the reduction of cement contents in concrete. In particular, limestone calcined clay cement (LC3) allows a clinker substitution of more than 45% without degradation of mechanical performance [9,10]. Indeed, the additional hydrates (ettringite, C-(A)-S-H) formed in the presence of alumina from the calcined clay contribute to the microstructure [11]. In addition to that, the limestone induces a filler effect [12] and its calcium carbonate reacts with the remaining alumina, precipitating carboaluminates, thus refining the porosity while also preventing the conversion of ettringite into monosulfoaluminates [13,14]. This material demonstrates a potential for 3D printing [15–17]. The calcined clay provides higher static yield stress and plastic viscosity at fresh state [18] as well as enhanced structuration rate [19]. These properties originate mainly from the reactivity of alumina, the platelet structure of clay, the higher specific surface area, and the negative surface charge of calcined clay [20].

* Corresponding author at: Navier Laboratory, École des Ponts ParisTech, Gustave Eiffel University, CNRS, Champ-sur-Marne, France.
E-mail address: zibo.jin@enpc.fr (W. Jin).

https://doi.org/10.1016/j.cemconcomp.2024.105853
Received 12 July 2024; Received in revised form 31 October 2024; Accepted 17 November 2024
Available online 26 November 2024

On the other hand, limestone filler reduces the yield stress and viscosity [21,22], offering an opportunity to tune the fresh state properties. However, these types of sustainable materials involve more diverse supplementary cementitious materials (SCMs) as well as chemical admixtures [23,24]. In the end, with the increased number of parameters and different chemical processes, **traditional mix design methods struggle to perform.**

Several mixture design methodologies are reported in the literature, all of which have strengths and weaknesses. Prescriptive proportioning methods consist in following guidelines from design methods [25]. These methods are simple but do not yet adapt to specific applications such as 3D printing or environmental optimization. Performance-based approaches rely on iterative trial formulations for mixture proportioning and remain the most straightforward, widespread procedure [2]. However, **the workload sharply increases with the number of parameters as well as the number of objectives.** In any case, these two strategies result in functional rather than optimal materials. On the other hand, computational design methods rely on mathematical relationships between independent variables as well as optimization algorithms [26]. In this category, multi-variable regression from empirical data is often applied [27] but efficient design of experiments is unfeasible for concrete mix design with more than 3 parameters. As a consequence, variables are often set constant, which limits the search space. **Mix design methods based on physical and chemical models require labor-intensive characterization** [28–30] (chemical composition, granulometry, water absorption, reactivity, and more) as raw materials are naturally different. The complexity of multi-scale modeling also reduces the reliability of predicted macroscopic properties. Finally, data-driven techniques rely on machine learning for the prediction of concrete properties [31,32]. Instead of physical or statistical equations, these approaches use large training datasets to update patterns between variables according to experimental results [33,34]. This method is simple to carry out and captures non-linearities. **However, when used for concrete mixture design, the variability in raw material chemical composition, reactivity, or processing, affects the reliability of published data for direct use with local materials** [35]. Furthermore, the volume of published data on 3D printable LC3 is insufficient for implementing a standard training strategy.

In order to respond to all these issues, the present paper proposes an optimization methodology which integrates fresh and hardened properties alongside the minimization of environmental impact as the paramount objective. Indeed, a multiobjective genetic algorithm is applied to a very low-clinker blended mortar by using a parametric life cycle assessment (LCA) model for the calculation of climate change (ClCh) score and artificial neural networks (ANNs) for the prediction of rheological and mechanical properties. These estimations serve as objective functions in an iterative optimization process using local materials and adaptable characterization methods. The use of an active learning technique for ANNs allows for greater predictions with a limited number of runs throughout unexplored design regions. Therefore, the natural variability of an increased number of parameters (limestone, calcined clay) is correctly handled. Additionally, ANNs integrate non-linearity with specific activation functions, the choice of which is optimized in this study. After the constitution of a training dataset, this methodology allows to rapidly identify mixture proportions generating low dynamic yield stress, high static yield stress, high thixotropy and minimized ClCh score. This optimization tool allows us to first determine a printable mixture with a reduced ClCh score compared to a reference mixture. In a second round of optimization, the presented methodology suggests a printable mixture with a specific higher compressive strength.

The entire optimization process is described in Section 1. The materials are presented in Section 2 along with the characterization protocol, the LCA framework, and the optimization tools. Afterwards, Section 3 depicts the preliminary results of the training dataset construction before introducing the optimization results. Finally, Section 4 analyzes the main takeaways and limitations of this mix design strategy.

1. Optimization methodology

The proposed optimization methodology aims at rapidly converging toward a narrow design region containing an optimized mixture. To do so, it combines the strengths of a multiobjective genetic algorithm and artificial neural networks for the ranking of computer-generated mortar mixtures based on environmental, rheological, and mechanical properties. In this section, the general methodology of this study is described, along with the requirements for its fulfillment.

The methodology involves the use of multiobjective optimization, widely used in a variety of sectors, including concrete mixture design [36–38]. In these problems, the outcome is a combination of solutions that constitute compromises between different objective functions rather than a single solution. The definition of these problems can be summarized by Eq. (1).

$$\text{Minimize } \{f_1(X), f_2(X), \ldots, f_k(X)\} \quad \text{for } X \in S \tag{1}$$

Where several conflicting objective functions, $f_k : \mathbb{R}^n \rightarrow \mathbb{R}$, where $k \geq 2$, must be simultaneously minimized. The decision variables X, in the form of vectors, belong to the solution region $S \subseteq \mathbb{R}^n$. The objective vector can be considered optimal if none of their components can be improved without compromising at least one of the others. In this case, it means no other solution is better in all objectives and this solution is called non-dominated. When it is on the theoretical boundary of optimal trade-offs (Pareto front), it is called Pareto-optimal [39].

This approach is implemented via a genetic algorithm named *Non-dominated Sorting Genetic Algorithm 2* (*NSGA-II*) [40]. This algorithm is widely used in multiobjective problems [36,38,41] and features several techniques to deal with constrained non-linear problems with numerous objectives. Particularly, it integrates elitism, an explicit diversity preserving mechanism, and a crowding distance fitness value. The *NSGA-II* algorithm generates a random population of mortar mixtures and sorts them via a binary tournament mating selection, according to their printability, mechanical properties and environmental quality. Then, a child population is created using crossover and mutation, introducing diversity in the solutions. Both populations are merged and a subset undergoes the same process over and over until a termination criterion is reached.

The Fig. 1 depicts the optimization process, which is explained here. The individuals generated by the genetic algorithm are mixtures composed of six constituents: Portland cement with silica fume (GUbSF), calcined clay (CC), limestone filler (LF), water (W), sand (Sa) and superplasticizer (SP) — More details are available in Section 2. As such, the mixture design space consists of a 6-dimensional decision vector X composed of these six independent variables x.

In our case, the objectives are to reach the printability thresholds, which consist in pumpability, extrudability and buildability criteria (definition in Section 2.2.3), to satisfy an optional strength requirement, and most importantly, to minimize the climate change score. In order to assess the quality of each individual, a computational evaluation is necessary to assign a fitness function $F(X)$, combination of objective functions $f_k(X_i)$. First, a contextualized parametric LCA model is developed to estimate the climate change score of individuals [42]. Then, for the physical characterization, artificial neural networks are trained to predict the rheological and mechanical properties with an appropriate local database (description in Section 2.2.4). Thus, the objective functions are the output of the LCA model (LCA CO_2), the compressive strength (ANN Strength), and the three rheological measurements used to evaluate printability, namely the flow (ANN Flow) and slump (ANN Slump) at respectively 2 and 6 min after mixing, as well as the structuration rate (ANN Athix) (description in Section 2.2.2).

An intermediate step is to determine the most adequate hyperparameters for ANN training through a single-objective optimization (described in Section 2.2.4). Finally, the experimental optimization is applied. **A method of active learning** is chosen to get progressively

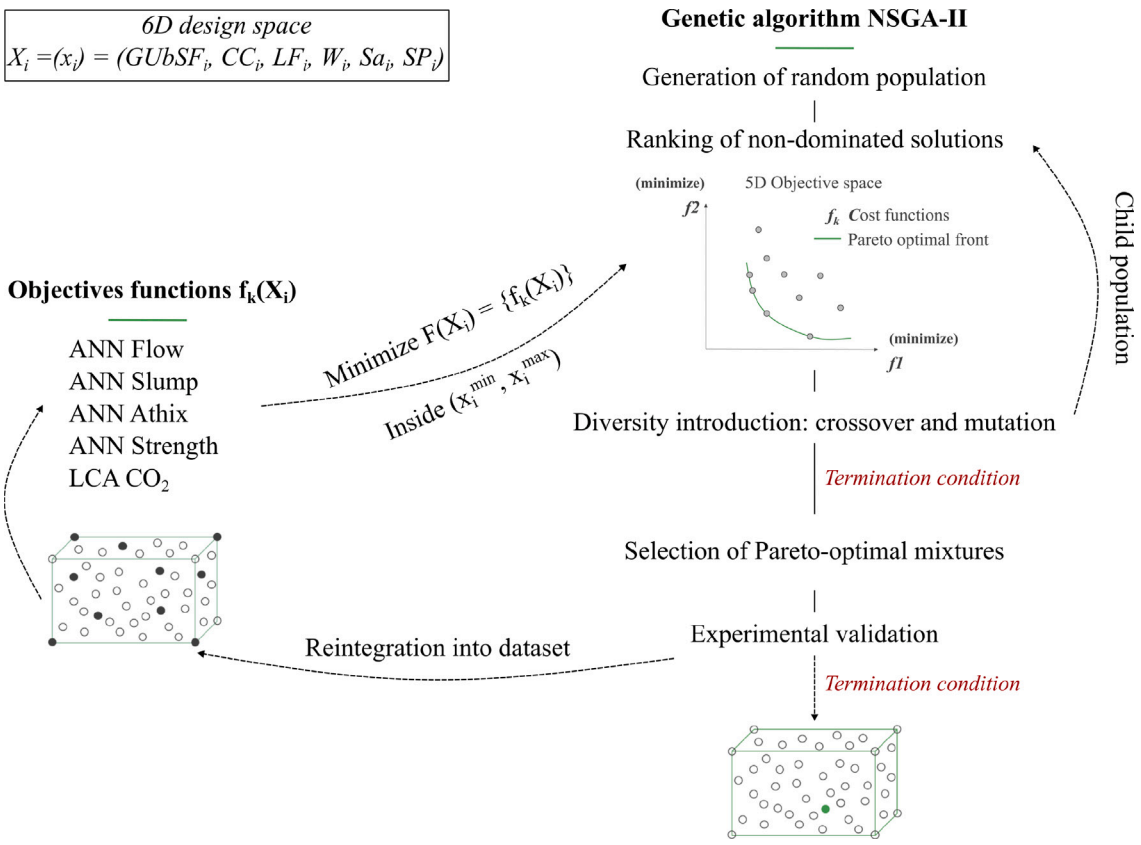

Fig. 1. Outline of experimental iterative optimization process.

Table 1
Complete summary of the optimization methodology.

Phase	Step	Description
Preliminary Steps	Step 1	Definition of printability thresholds through literature review and large-scale 3D printing
	Step 2	Trial-and-error campaign: Determination of a design region with measurable physical properties and GWP reduction
Definition of objective functions	Step 3	Constitution of parametric LCA model
	Step 4	Implementation of an optimized design of experiments as training dataset
	Step 5	Optimal training of ANNs for predicting rheological properties
Experimental optimization	Step 6	Definition of the search space, meaning parameter boundaries
	Step 7	Application of a multiobjective genetic algorithm for minimizing ClCh score within printability and mechanical constraints
	Step 8	Selection of three solutions for experimental validation and integration of results into the experimental database
	Step 9	Repeat steps 5 to 9 until constraints are satisfied with minimized ClCh score

better predictions as the study progresses. After applying the genetic algorithm, three solutions in the Pareto-optimal space are selected to be reproduced experimentally. The physical results for these mixtures are then reintegrated into the training dataset, thus improving the predictions in the explored design regions. This operation is then repeated until a satisfactory mixture is found. Thereafter, the design region can be progressively expanded, allowing us to determine a local optimum. Particularly, the design region is enlarged when the best outputs of the genetic algorithm tend toward the boundary limits, thus meaning the search space is potentially too constrained.

In the end, the complete optimization process can be summarized in 9 steps (Table 1). The preliminary steps 1 (definition of printability thresholds) and 2 (determination of a relevant design region for the research) are covered in Section 2.2.3. The definitions of objective functions are stated in step 3 for the LCA (detailed in [42]) and in steps 4 and 5 for rheological properties (presented in the Section 3.1). Finally, the results of the experimental and iterative optimization (steps 6, 7, 8 and 9) are detailed in Sections 3.2 and 3.3.

In the following section, all materials and methods relevant to the execution of this optimization process are reported: the constituents of our quaternary blend; the application of our contextualized LCA model; the test procedures for printability and mechanical strength; the definition of printability based on a literature review and large-scale experiments; the collection of training data using a design of experiments; the tuning of hyperparameters for each ANN training.

2. Materials and methods

In this section, the materials constituting our quaternary LC3-based blend are listed. Moreover, the characterization protocol, the LCA framework and the definition of printability are explained, all of which serve as input variables in the genetic algorithm.

2.1. Materials

The binder is composed of three powder elements: cement blended with 8.3% silica fume (42.5 MPa) in accordance with the CSA A3001 standard, calcined clay (80% metakaolin) Class N natural pozzolan conforming to both the CSA A3000 and ASTM C618 standards, and limestone filler. The sand is kiln-dried with a maximum particle size

Table 2
List of materials used and composition of reference mixture of 30.5 MPa.

Material	Abbreviation	Supplier	Reference mix (kg/m^3)
Cement blended with silica fume	GUbSF	Ciment Québec	165
Calcined clay	CC	Whitemud Resources	132
Limestone filler	LF	Graymont	362
Water	W		237
Sand	Sa	Bomix	1317
PCE Superplasticizer	SP	Master Builders	6.59

Table 3
Chemical compositions of binder components.

(m%)	GUbSF	CC	LF
SiO_2	27.0	62.5	2.21
Al_2O_3	4.2	31	0.37
Fe_2O_3	1.6	1.1	0.14
CaO	57.5	0.4	53.6
MgO	1.6	0.3	0.51
SO_3	3.6	0	0.1
TiO_2	0	0.6	0.01
Na_2O	0.73	0.16	0.02
K_2O	0	1.81	0.13
Loss on ignition	3	0.95	42.9

of 2.5 mm and the superplasticizer is based on polycarboxylate-ether, meeting the ASTM C494 requirements for Type A, water-reducing, and Type F, high-range water-reducing admixtures. The abbreviations and suppliers are listed in the Table 2. The mixture resulting from the preliminary phase (steps 1 and 2 in Table 1) is reported in the column *Reference mix*. **This formulation satisfies the printability thresholds defined in** Section 2.2.3 **with a compressive strength of 30.5 MPa at 28 days.** More details are available in Section 2.2.3.

The oxide composition of the binder materials are listed in the Table 3. The specific gravity for the GUbSF, the calcined clay, the limestone filler and sand are respectively 3.15, 2.74, 2.63, and 2.68.

2.2. Methods

To apply the optimization process, several components are needed for the definition of the objective functions :

- Characterization protocols for ClCh score and physical properties;
- Specification of printability requirements at fresh state;
- Procedure for ANN training;
- Methodology for active learning optimization process.

2.2.1. Life cycle assessment

The climate change score is calculated with a cradle-to-gate LCA model using Python software *Brightway2* [43]. The printing, use phase, and end of life are excluded from this calculation as well as the laboratory infrastructure. The functional unit is the **production of 1 m^3 of 3D printing material**. The life cycle impact assessment method *EF 3.0 baseline model of 100 years* is used as recommended by the International Reference Life Cycle Data System [44]. The information pertaining to this model is extensively reported in [42].

2.2.2. Test procedures

The printability is defined through three phases with different ranges of static and dynamic yield stresses. First, the pumpability is evaluated after mixing, then the shape retention is assessed at the time of deposition. Finally, measurements of static yield stress in the first hour generate a structuration rate characterizing the buildability.

The flow table test is carried out 2 min after mixing (ASTM C1437 [45]). A truncated cone is filled in two layers, each compacted 20 times with a rubber rod. It is lifted and the table is dropped 25 times in 15 s at a steady pace. The resulting dimension of the sample is measured with a caliper along the four lines of the flow table. The sum of the four readings is the increase in diameter compared to the base diameter of the cone, within 0%–152%. The slump test is performed 6 min after mixing according to the standard [46]. A miniature version of the Abrams cone (base diameter 100 mm - top diameter 50 mm - height 150 mm) is filled in three layers, each tampered 25 times with a metal rod. It is then lifted in 5 s, letting the mortar slump under self-weight. The resulting static yield stress is estimated with Eq. (2) [47].

$$\tau = \frac{\rho g (H_0 - s)}{\sqrt{3}} \tag{2}$$

With τ the yield stress, ρ the density, g the gravitational constant, H_0 the initial height of the sample and s the slump.

Concerning the structuration rate, Roussel et al. [5] suggests a linear model of yield stress evolution in the dormant period, introducing a parameter named *Athix*, which represents the ability of cementitious materials to build an internal structure at rest. This model is confirmed for the measurements in this paper. With this assumption, the build-up rate requirement assuming a constant elevation rate h_z is as follows:

$$\tau_0 + (Athix - \frac{\rho g h_z}{\sqrt{3}})t > 0 \tag{3}$$

To calculate this *Athix* in the first hour, we measure the yield stress at 30 and 60 min using the direct shear test [48]. The latter, generally used in the geotechnical field was applied to 3D printing mortars [49,50], permitting a discrete assessment of yield stress in the tens of kPa under pure shear. A mortar sample is placed in two layers, compacted on a vibrating table for 5 s, inside a circular shear box composed of a top and a bottom part. This box is then loaded onto a *Humboldt* direct shear testing machine equipped with a linear displacement motor, a displacement sensor, and a 100 kN load cell. During the test, the top part is free to move horizontally at a rate of 12.7 mm/min, transmitting a shear load through the specimen. Each test runs for less than 1 min until the sample fails on the predetermined horizontal plane corresponding to the dimensions of the shear box. As the shearing proceeds, the surface corresponding to the intersection of the top and bottom parts of the box changes according to Eq. (4) where A_c is the corrected section, A_i is the initial section, δ_h is the horizontal displacement, and D is the diameter of the shear box. The shear stress τ is thus obtained from Eq. (5) with F being the force measured by the sensor.

$$A_c = A_i \left[\frac{1}{90} \cos^{-1}\left(\frac{\delta_h}{D}\right) - \frac{2}{\pi}\frac{\delta_h}{D}\sqrt{1 - \left(\frac{\delta_h}{D}\right)^2} \right] \tag{4}$$

$$\tau = \frac{F}{A_c} \tag{5}$$

Consequently, a linear regression between the yield stress value obtained through the slump test at 6 min and the shear stresses at 30 and 60 min provides a structuration rate $Athix$ in Pa/s, corresponding to the slope.

The compressive strength is determined on three cubic 50 mm samples molded in 2 layers, each compacted 32 times with a rubber rod, according to the standard ASTM C109 [51]. After a cure of one day in the mold, the samples are placed in a curing chamber with a temperature of 22 °C and a relative humidity of 97.5% for a total cure of 28 days. For the test, a compression machine equipped with a hydraulic piston is used at a constant pace rate of 1 kN/s until the specimen fails. The maximal load applied constitutes the compressive strength of the mixture. Tested samples are depicted on the Fig. 2.

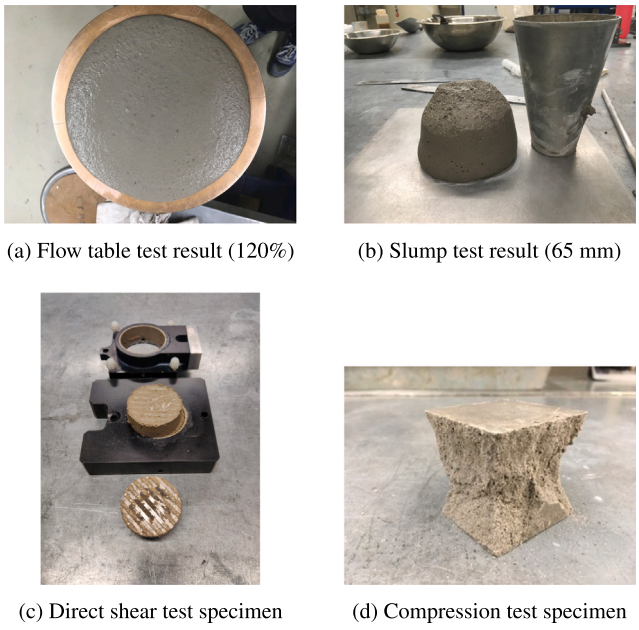

(a) Flow table test result (120%) (b) Slump test result (65 mm)

(c) Direct shear test specimen (d) Compression test specimen

Fig. 2. Samples after test procedures at fresh state and compressive strength.

2.2.3. Printability

The mixtures are formulated for a continuous mixing system which involves a one-component mortar mixing pump (MAI 4MULTI-MIX) and a 6-axis industrial robot (ABB IRB 6620). The 3D printing protocol consists of multiple steps: designing and slicing a 3D model on the software *Rhinoceros* with the parametric design plugin *Grasshopper*, before converting the robot path into *RAPID* code; Having prepared all the dry materials in 20 kg bags, they are poured in the *4MULTIMIX* hopper and mixed with water and superplasticizer; The mortar is conveyed to the robot printing head and deposited.

Considering this setup, the test procedures in Section 2.2.2 allow us to estimate the quality of each mixture formed. The printability objectives were first identified in the literature. The latter shows a correlation between the flow test and pumpability, and places the flow threshold at very different values. Several studies mention a value between 150 and 210 mm [52–55] while others specify values below 110 mm [49,56,57]. The extrudability criterion is assessed by Khan [58], Chen et al. [59], Cho et al. [52] and Liu et al. [60], who indicate an optimum static yield stress at deposition of respectively 300–2500 Pa, 590–895 Pa, 940–6802 Pa and 1113–1658 Pa.

A first assessment with the printing equipment available at École de Technologie Supérieure [61] placed the rheological requirements at 125% flow and 80 mm slump. A trial and error process for determining an appropriate quaternary system resulted in a material satisfying these criteria. The resulted print exhibits an optimal yield stress τ at 17 min after mixing, which corresponds to adequate pumpability and excellent shape retention, as illustrated on the Fig. 3. Within this timeframe, the flow test and the slump test are reproduced for the mixture and define the appropriate objectives for our extrusion system: 104% flow and 65 mm slump. A margin for the flow is considered as the pumping equipment is highly sensitive to variations in the entry material.

Consequently, we consider in this study a flow threshold of 120% (220 mm) which is a conservative value. Additionally, the threshold value of 65 mm slump at deposition corresponds to a critical yield stress of 1059 Pa (Eq. (2)). It guarantees the stability of more than 10 layers of mortar with a thickness of 8 mm according to Eq. (3), even when neglecting the build-up rate of the material. This ensures constructibility in the first few minutes of printing. Finally, the criterion for the structuration rate originates from an arbitrary, realistic goal corresponding to an elevation of 1 m at 60 min. Considering a density of 2.2, a layer length of 2 m, a flow rate of 1 L/min, and a printing speed of 69 mm/s, the elevation rate is 0.276 mm/s. The Eq. (2) gives a requirement of 12.5 kPa at 60 min for the first layer, which consequently leads to a 3.5 Pa/s Athix if we consider the yield stress requirement at deposition (1059 Pa at 6 min).

A second trial and error process was conducted, for a total of 22 mixtures, to determine a proper quaternary blend, which is called the Reference mix in the Table 2. The characterization tests and printability thresholds are summed up in the Table 4. The whole printability requirements and hypotheses are represented on Fig. 4.

2.2.4. ANN training

To evaluate the quality of randomly generated mixtures (populations), ANNs serve as prediction tools for the test procedures defined in the previous section. A training dataset is constituted using a D-optimality criterion [62] for an 18-run design of experiments (DoE) with six factors (mass fractions of constituents) and three levels. This type of design represents the widest volume in the search space for a given number of experiments by maximizing the determinant $D = |X^T X|$ of the information matrix $X^T X$. Optimal DoE quality corresponds to a balanced and orthogonal design if it exists, i.e. if $(X^T * X)^{-1}$ is diagonal and equal to $\frac{1}{N_D} I$.

With the results of this DoE, ANNs are trained to predict the flow, the slump, the structuration rate, and the compressive strength. For each training, using the *NSGA-II* algorithm, the most efficient hyperparameters are determined through the simultaneous maximization of coefficient of determination (R^2) and minimization of normalized root mean square error ($RMSE$) for the validation set (equation (6) and (7)).

$$RMSE = \sqrt{\frac{1}{n}\sum_{i=1}^{n}(y_i - \hat{y}_i)^2} \tag{6}$$

Fig. 3. Resulting print using an initial mixture: the decreasing plastic deformation at deposition, from $\tau <$ critical yield stress τ_{cr} (in red) to $\tau >$ pumping limit τ_p (in red) illustrates the structuration rate. (For interpretation of the references to color in this figure legend, the reader is referred to the web version of this article.)

Table 4
Test methods and printability thresholds.

Property	Test method	Printability requirement
Pumpability	Flow table test [45] at 2 min	≥ 120%
Shape retention	Slump test [46] at 6 min	= 65 ± 5 mm
Buildability	Direct shear test [48] at 30/60 min	≥ 3.5 Pa/s

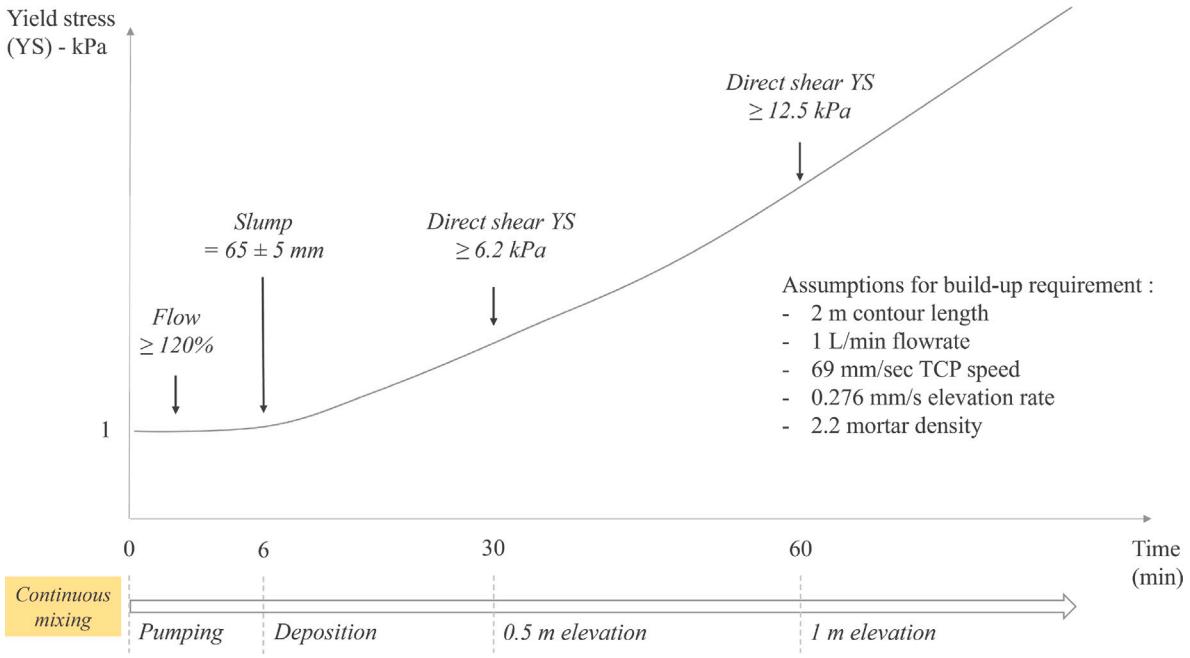

Fig. 4. Printability requirements considering a continuous mixing unit: thresholds for flow, slump and direct shear yield stress values.

$$R^2 = 1 - \frac{\sum_{i=1}^{n}(y_i - \hat{y}_i)^2}{\sum_{i=1}^{n}(y_i - \bar{y})^2} \quad (7)$$

where $\hat{y}_i$ is the predicted value, y_i is the actual value, $\bar{y}$ the mean of the observed data and n the number of data points.

The assessed hyperparameters are the activation function, learning rate, number of layers, and number of neurons in each layer. The available activation functions are *exponential linear unit* (elu), *scaled exponential linear unit* (selu), *rectified linear unit* (relu), *hyperbolic tangent activation function* (tanh), *sigmoid activation function* (sigmoid), *softmax activation function* (softmax), *softplus activation function* (softplus), *softsign activation function* (softsign) and *exponential activation function* (exponential). The learning rate, number of layers and number of neurons are respectively set between [0.001 – 0.003], [1 – 5] and [1 – 400]. Each time, the best combination of hyperparameters is saved and used in the evaluation of *NSGA-II* populations. The package *tensorflow* is used for the ANN, *pymoo* for the genetic algorithm and the *Matlab* function *rowexch* for the generation of a D-optimal DoE.

2.2.5. Multiobjective computation

The determination of non-dominated solutions is carried out using the Python library *pymoo*, which implements the *NSGA-II* genetic algorithm. User inputs are necessary for the definition of independent variables boundaries and for the selection of the best performing solutions. In our case, the design space was progressively expanded as the study progressed to reflect the tendencies of the suggested mixtures (Tables 6 and 8).

3. Results

3.1. Design of experiments and ANN training

The 18 experimental results of the design of experiments (DoE-1 to 18) are presented in the Table 5. The results for the flow, slump, Athix, and strength span respectively from 76% to 152%, 0 to 150 mm, 3.1 to 4.0 Pa/s, and 25.8 to 34.6 MPa. From these data points, we observe that the increase in sand proportion significantly influences the flow and slump results. These trends indicate the importance of the paste/aggregate ratio, which governs the flow regime. In these conditions, this factor determines the transition from hydrodynamical flow (enough paste to coat the aggregates) and frictional regime (highly dissipative interactions) with a sharp increase in yield stress for the second case [63]. On the other hand, the Athix and strength values are impacted respectively by calcined clay and cement contents, as expected in this design. With this database, the iterative optimization depicted on Fig. 1 can be carried out.

3.2. Iterative optimization without strength consideration

The iterative optimization process depicted on Fig. 1 is detailed before presenting the results. The selected objectives for this study center around the reduction of the ClCh score. The first optimization round aims at reducing the ClCh score without consideration of the compressive strength. The purpose is to illustrate the efficiency of this optimization methodology at tuning multiple objectives.

The explicit objectives are to reach 120% flow, 65 mm slump, 3.5 Pa/s Athix and to minimize the ClCh score. For this, 9 mixtures were formed in the iterations i1 to i3. Then, the search space was expanded and 6 additional mixtures were formed in the iterations i4 and i5. The parameter boundaries are listed in the Table 6 and the optimization sequence is depicted on Fig. 5.

The Table 7 reports the results for the suggested mixtures, the 3 mixtures for each iteration are denoted as ix-1, ix-2 and ix-3, with $x = 1, \ldots, 5$. The columns pF, pS, pA are respectively the predicted flow, slump, and Athix. The columns mF, mS, mA are the measured flow, slump, and Athix. Afterwards, the results for each experimental

Table 5
Results of D-optimal design of experiments — Abbreviations of the 6 independent variables are in Table 2.

Mix	GUbSF	CC	LF	W	Sa	SP	Flow	Slump	Athix	Strength
	kg/m^3						%	mm	Pa/s	MPa
DoE-1	164	132	362	246	1315	7,17	152	120	3,3	31,5
DoE-2	148	118	367	227	1334	6,29	106	51	3,6	26,7
DoE-3	161	137	353	252	1285	6,84	141	100	3,1	27,6
DoE-4	145	123	339	222	1306	6,00	99	35	4,0	26,8
DoE-5	151	136	353	237	1282	6,57	128	85	3,5	25,8
DoE-6	151	136	375	226	1286	6,27	78	24	4,1	28,8
DoE-7	163	122	336	234	1302	6,34	132	87	3,4	30,3
DoE-8	155	117	342	229	1316	6,37	126	78	3,1	29,8
DoE-9	160	128	353	225	1284	6,42	99	42	3,4	29,9
DoE-10	166	133	386	244	1245	6,46	116	62	3,4	30,6
DoE-11	157	133	325	221	1334	6,29	77	20	3,6	30,3
DoE-12	164	139	383	237	1235	6,73	104	61	3,9	31,4
DoE-13	178	126	370	236	1263	6,55	116	73	3,6	34,6
DoE-14	169	120	373	236	1278	6,39	122	69	3,3	32,7
DoE-15	171	129	334	233	1293	6,63	120	77	3,6	34,5
DoE-16	163	123	359	216	1304	6,31	76	0	3,5	33,8
DoE-17	164	131	321	229	1315	6,04	90	34	3,6	29,8
DoE-18	176	141	366	239	1250	6,64	118	73	3,7	32,8

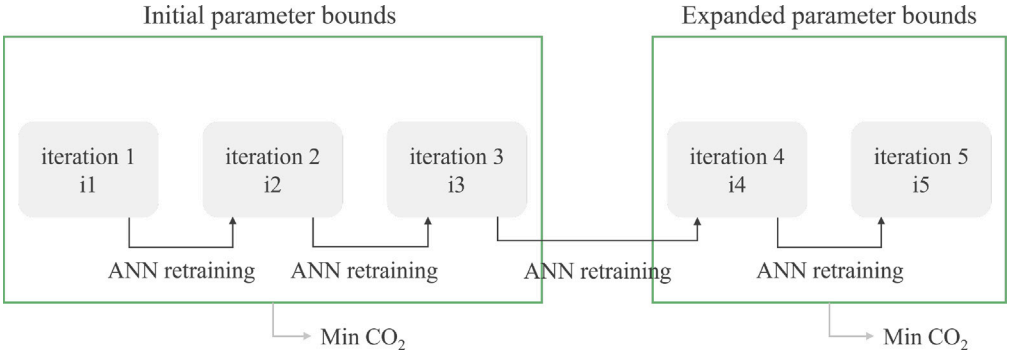

Fig. 5. Illustration of the first optimization sequence. The explicit objectives are to reach 120% flow, 65 mm slump, 3.5 Pa/s Athix and to minimize the ClCh score.

Table 6
Boundaries of independent variables for the genetic algorithm: iterations i1-i3 and i4-i5.

Parameter	Initial boundaries (kg/m^3)	Expanded boundaries (kg/m^3)
GUbSF	140–180	120–180
CC	110–150	90–150
LF	340–380	340–400
W	210–250	200–260
Sa	1200–1400	1200–1450
SP	5.5–7.5	5.5–8

iteration is described. Each time, the coefficients of correlation $R^2$for all training and testing data are mentioned for flow, slump, Athix and strength predictions.

For the **first iteration**, the ANNs for flow, slump, and Athix are trained with a 27-mixture dataset ($\{R^2_{flow}, R^2_{slump}, R^2_{Athix}\} = \{0.96, 0.94, 0.70\}$), comprised of the trial-and-error and the DoE. As the genetic algorithm proposes solutions in unseen design regions, the ability of ANNs to generalize is known to be inefficient with such a small dataset. Thus, the errors compared to the predictions, as well as the printability objectives are substantial, even with limited ClCh score reduction. The ANNs tend to underestimate the flow and slump with respective mean errors of 23% and 43 mm across the three mixtures. On the other hand, they slightly overestimate the Athix with a mean error of 0.3 Pa/s. These errors are expected to decrease throughout the iterations when the optimal design region is identified.

For the **second iteration**, the ANNs are trained with a 30-mixture dataset ($\{R^2_{flow}, R^2_{slump}, R^2_{Athix}\} = \{0.96, 0.92, 0.76\}$). We decided to explore higher ClCh score reduction regions (up to 13% compared to the reference material) by forming mixtures with decreased proportions of reactive products, thus giving low Athix predictions. This choice was made to provide the ANNs with data points in this experimental space, which represents the minimal ClCh score region. Again, as seen in the Table 7, errors are significant in this unseen region with mean errors of 34%, 43 mm and 0.8 Pa/s respectively for flow, slump, and Athix. With these ANNs, the flow and slump as well as the Athix are underestimated in the lower CC proportions. In the end, the Athix threshold is not reached in this iteration.

For the **third iteration**, the ANNs are trained with a 36-mixture dataset ($\{R^2_{flow}, R^2_{slump}, R^2_{Athix}\} = \{0.96, 0.85, 0.79\}$). Different combinations of CC, LF, W, Sa, and SP values are investigated. A significant increase in prediction quality is observed with mean errors of 11%, 26 mm, and 0.2 Pa/s respectively for flow, slump, and Athix. The mixture i3-1 confirms the difficulty in reaching the Athix threshold with a CC content close to the lower boundary (110 kg/m^3). The mixture i3-2, although failing to reach the flow threshold, displays enhanced Athix with less than 5.8 wt% of CC. On the contrary, the mixture i2-3 reached only 3.0 Pa/s with 6.2 wt% CC. This is due to the decreased W/binder ratio (0.313), and more specifically W/CC ratio (1.79) for i3-2, compared to i2-3 (0.370 W/binder, 1.93 W/CC). On the other hand, the mixture i3-3 reaches all the printability constraints with a 6% ClCh score reduction. This mixture constitutes a local optimum, however, it involves a high W/binder ratio (0.388) and a GUbSF content close to the lower boundary defined in this first optimization round.

Considering these results, the design region is expanded in an attempt to improve the minimization of the ClCh score for this 3D printing material. A lower constraint of 120 kg/m^3 GUbSF is set, expanding the search space but ensuring a minimal compressive strength. For the **fourth iteration**, the ANNs are trained with a 39-mixture dataset ($\{R^2_{flow}, R^2_{slump}, R^2_{Athix}\} = \{0.95, 0.85, 0.80\}$), the parameter

Table 7
First round of suggested Pareto-optimal solutions: Parameter boundaries are in Table 6, each iteration includes 3 mixtures denoted ix-1 to ix-3.

Mix	GUbSF	CC	LF	W	Sa	SP	ClCh	pF	pS	pA	mF	mS	mA
	kg/m^3						kg CO_2-eq	%	mm	Pa/s	%	mm	Pa/s
i1-1	148	131	348	239	1346	7.27	239	113	66	3.3	148	114	3.4
i1-2	169	112	352	223	1347	6.68	240	116	42	3.5	128	95	3.3
i1-3	171	111	343	240	1352	6.59	243	121	75	3.0	144	102	2.4
i2-1	148	113	366	248	1318	5,67	225	118	64	1,8	136	83	2,9
i2-2	141	111	373	249	1346	6,46	219	110	65	1,2	152	115	2,2
i2-3	142	137	368	248	1329	7,19	241	111	65	3,3	152	125	3,0
i3-1	143	113	344	238	1372	6.88	222	120	65	2,6	148	105	2,5
i3-2	143	127	379	212	1331	7.33	233	115	43	3,7	111	73	4,1
i3-3	140	138	342	249	1298	5.57	236	122	55	3,3	120	64	3,5
i4-1	127	95	367	249	1381	7.24	198	105	68	1,2	152	119	1,8
i4-2	121	132	385	215	1330	7.45	219	101	44	3,7	96	39	4,5
i4-3	126	143	345	237	1314	6.32	231	108	65	3,3	99	41	3,7
i5-1	122	112	365	211	1393	8.07	204	108	47	4,0	87	34	3,2
i5-2	126	120	368	229	1368	7.98	212	127	78	3,6	139	110	3,5
i5-3	126	140	376	232	1324	7.37	226	120	62	3,6	119	66	4,3

boundaries are listed in the Table 6. To identify a suitable search space, several low GUbSF (< 5.3 wt%) design regions are explored with this iteration, one with low CC (4.3 wt%) and high W/binder ratio (0.407), one with average CC (6 wt%) and low W/binder ratio (0.323), and one with high CC (6.6 wt%) and average W/binder ratio (0.372). Average errors of 20%, 26 mm, and 0.6 Pa/s are recorded for the flow, slump, and Athix, which are higher than the previous iteration due to the assessment of an unseen optimization region. It can be deduced from the last three iterations that a certain proportion of CC is necessary for reaching the Athix threshold set in Table 4. Also, even with more SP, the mix i4-2 seems to be in the frictional flow regime (0.323 W/binder ratio, 1.56 Sa/paste ratio) whereas the mix i4-3 also fails to reach a high enough flow, seemingly due to the higher CC content.

For the **fifth iteration**, the ANNs are trained with a 42-mixture dataset ($\{R^2_{flow}, R^2_{slump}, R^2_{Athix}\} = \{0.94, 0.92, 0.75\}$). Again, a decrease in average error is observed compared to the previous iteration with 11%, 16 mm, and 0.6 Pa/s respectively for flow, slump, and Athix values. The mixture i5-1 tends toward the respectively lower and higher boundaries for water and SP. In this case, the flow, slump, and Athix are overestimated, making the mixture too dry. On the other hand, the mixture i5-2 has a high slump and does not reach the Athix threshold. Finally, the mixture i5-3 satisfies the printability thresholds with a 10% reduction in the ClCh score compared to the reference material. In that case, the Athix is considerably higher than the defined objective, providing an improved buildability but higher than the optimal ClCh score. Thus, a mixture with less CC could constitute a local optimum. Nevertheless, the goal of significantly reducing the ClCh score without impacting the printability of our quaternary system is attained.

In order to provide a complete mix design tool, a compressive strength threshold is added as an objective. Thus, the next section presents the results for the minimization of GWP for a 40 MPa 3D printing LC3-based blend.

3.3. Iterative optimization with a strength target of 40 MPa

To propose an actual decrease of the ClCh score, the compressive strength needs to be taken into account. The second optimization round includes a compressive strength criterion, showing the number of additional mixtures formed for the identification of a higher-strength 3D printing material with a minimized ClCh score. The Table 8 details the independent variable boundaries and Fig. 6 illustrates this optimization sequence.

The Table 9 reports the results for the suggested mixtures, the 3 mixtures for each iteration are denoted as ix-1, ix-2 and ix-3, with $x = 6, \ldots, 9$. The predicted and measured properties of these Pareto-optimal solutions now include a strength criterion (predicted pR and measured mR).

Table 8
Boundaries of independent variables for the genetic algorithm: iterations i6 and i7-i9.

Parameter	Initial boundaries (kg/m^3)	Expanded boundaries (kg/m^3)
GUbSF	120–180	120–220
CC	90–150	90–170
LF	340–400	320–420
W	200–260	180–250
Sa	1200–1450	1200–1450
SP	5.5–8	5.5–10

For the **sixth iteration**, the parameter boundaries were left unchanged from the previous iterations and the ANNs are trained with a 45-mixture dataset ($\{R^2_{flow}, R^2_{slump}, R^2_{Athix}, R^2_{strength}\} = \{0.97, 0.90, 0.75, 0.73\}$). The results have low strength compared to the objective of 40 MPa and the respective predictions. Besides, average errors of 55%, 39 mm, 1.1 Pa/s, and 5.0 MPa are observed with the mixtures. These significant errors are due to the addition of the 40 MPa strength objective. Indeed, the algorithm suggests solutions with higher cement content, meaning design regions with minimal representation in the training dataset. Overall, the need for an expansion of the design region is clear considering the compressive strength results. Thus the GUbSF higher limit is set to 220 kg/m^3 for the next iterations.

The ANNs are trained with a 48-mixture dataset in the **seventh iteration** ($\{R^2_{flow}, R^2_{slump}, R^2_{Athix}, R^2_{strength}\} = \{0.90, 0.90, 0.78, 0.77\}$). The latter explores again three W/binder ratio ranges (0.339, 0.351, and 0.300 for respectively i7-1, i7-2, and i7-3) with also an increase in paste volume for i7-3. Average errors of 15%, 32 mm, 1.2 Pa/s, and 1.6 MPa are reported respectively for flow, slump, Athix, and strength, which is overall lower than the previous iteration. For the mixture i7-1, the ANNs properly capture the variable interactions although the strength threshold is not met for the desired application. On the contrary, the ANNs for mixtures i7-2 and i7-3 overestimate the flow properties.

Concerning the **eighth iteration**, for which ANNs are trained with a 51-mixture dataset ($\{R^2_{flow}, R^2_{slump}, R^2_{Athix}, R^2_{strength}\} = \{0.91, 0.82, 0.65, 0.78\}$), lower W/binder ratios are investigated. The average errors for the four experimental procedures are 5%, 39 mm, 0.2 Pa/s, and 1.0 MPa, which shows a challenge to predict slump results in this design space. Overall, this iteration demonstrates a struggle to decouple flow and slump outputs, possibly within these low W/binder regions (0.275 to 0.286), which require higher SP contents.

Finally, the **ninth iteration** is trained with a 54-measurement dataset ($\{R^2_{flow}, R^2_{slump}, R^2_{Athix}, R^2_{strength}\} = \{0.84, 0.86, 0.88, 0.71\}$). Three suggested mixtures are formed with average errors of 6%, 8 mm, 0.2 Pa/s, and 0.9 MPa between predictions and measurements. The predictions are accurate and show the ability of the ANNs to adapt to the previous results, allowing the *NSGA-II* algorithm to decouple flow

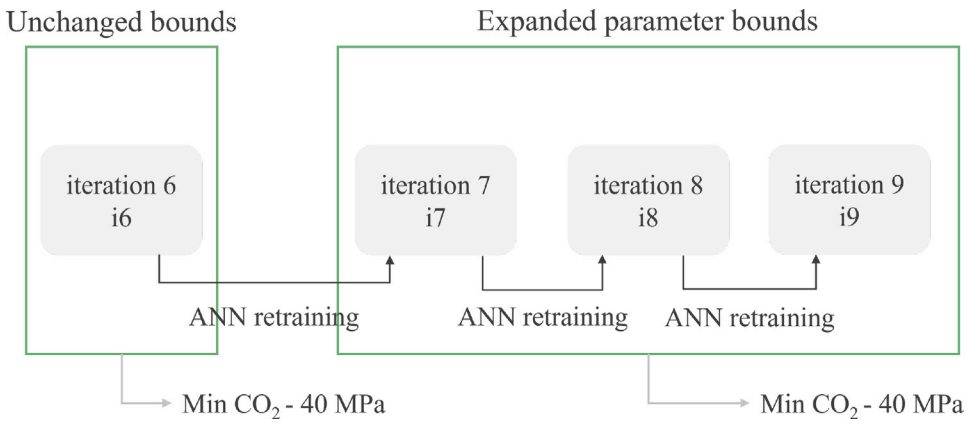

Fig. 6. Illustration of the second optimization sequence. The explicit objectives are to reach 120% flow, 65 mm slump, 3.5 Pa/s Athix, 40 MPa and to minimize the ClCh score.

Table 9
Second round of suggested Pareto-optimal solutions: Parameter boundaries are in Table 8, each iteration includes 3 mixtures denoted ix-1 to ix-3.

Mix	GUbSF	CC	LF	W	Sa	SP	ClCh	pF	pS	pA	pR	mF	mS	mA	mR
	kg/m^3						kg CO_2-eq	%	mm	Pa/s	MPa	%	mm	Pa/s	MPa
i6–1	180	96	334	212	1395	5.85	242	133	27	2.7	37.9	33	✗	✗	31.7
i6–2	176	131	331	231	1291	6.86	267	116	85	3.3	37.4	102	37	3.5	34.0
i6–3	173	145	370	218	1279	7.65	276	114	54	3.8	39.9	63	12	4.3	34.5
i7–1	186	134	335	230	1289	7.64	279	113	54	3.5	37.7	122	60	4.1	37.2
i7–2	195	150	321	242	1304	8.84	298	120	61	3.8	38.3	142	120	2.8	38.4
i7–3	199	139	413	234	1233	8.09	283	139	96	1.1	39.2	152	126	3.2	43.5
i8–1	212	145	368	208	1292	8.86	300	123	64	4.1	45.6	116	105	4.0	46.2
i8–2	215	145	362	213	1287	8.67	303	124	61	4.1	46.1	122	112	4.1	46.3
i8–3	194	112	397	210	1304	7.81	261	130	87	3.5	39.9	124	113	3.0	42.1
i9–1	200	123	366	237	1285	7.48	270	116	66	2.7	39.6	126	68	2.7	40.0
i9–2	199	128	360	232	1291	6.86	280	125	55	3.4	40.2	127	70	3.5	40.0
i9–3	205	127	371	227	1278	6.83	286	124	69	3.5	42.1	118	60	3.1	40.2

and slump properties by proposing solutions with increased W/SP ratio. Particularly, the mixture i9-2 satisfies every threshold while keeping the ClCh score below 280 kg CO_2-eq/m^3. As the suggested proportions do not tend toward any boundary conditions, an additional expansion of the design region is not required.

The Fig. 7 represents the measured values versus the predictions for flow, slump, Athix, and strength. The colors show the progress inside each optimization sequence, such as the red points depict the start of a round (change of objectives or search space) and the blue points illustrate the end of a sequence (i3, i5 or i9). Overall, these figures show that the predictions are scarcely accurate, as expected for small datasets. Still, as the optimization progress advances, the blue dots tend toward the green areas representing the physical objectives. On the other hand, when a red point shows a favorable result for a rheological test, it exhibits poor physical properties in other objectives. This can be illustrated by the highlighted mixture i6-2, which demonstrates appropriate Athix but unsuitable flow, slump and strength. In the same way, the mixture i7-1 shows adequate flow, slump and Athix, but insufficient strength. Nonetheless, this approach generates suitable mixtures and meet our objective to build a mixture design tool, without claiming the development of generalized predictive models.

3.4. Analysis of error profile

Overall, we carried out 9 iterations each comprising 3 mixtures. To visualize the evolution of mixture quality iteration after iteration, the average error per iteration compared to the ANN predictions as well as the objective thresholds are listed in the Table 10. The predictions columns *Flow-pred, Slump-pred, Athix-pred and Strength-pred* are normalized according to the ANN prediction value. The errors compared to the objectives *Flow-obj, Slump-obj, Athix-obj and Strength-obj* are normalized with respect to the rheological criteria in Section 2.2.3 (120%, 65 mm, 3.5 Pa/s) and the 40 MPa compressive strength threshold. The average errors compared to the ANN predictions (*Average-pred*) and physical objectives (*Average-obj*) are also listed. **The Fig. 8 represents the average experimental errors (*Flow-pred, Slump-pred, Athix-pred, Strength-pred*) compared to ANN predictions for each iteration**, along with the linear regressions of overall errors (*Average-pred*) inside each optimization sequence.

On Fig. 8, as expected, the changes in search space (i4) or objectives (i6) sharply increase the error, as the genetic algorithm explores unseen design regions. Nevertheless, the average error across all tests (red line) displays a rapid decrease inside each optimization sequence. Looking at individual tests, the errors seem high, especially for the slump test, however, as all conflicting objectives are pursued at the same time, the decrease in overall error is the key takeaway.

As the optimization process advances, more and more data is used for the training, logically reducing the errors. That being said, we believe this study shows the ability of this methodology to quickly converge below a certain error threshold, and more importantly converge toward the satisfaction of multiple conflicting objectives for a 3D printing mortar. Indeed, the error profiles within iterations i1-i3, i4-i5, and i6-i9 show that in four to five iterations, the ANNs can adapt to a new search space and determine a design region containing a printable material. Even more so, the decrease in errors allows the quick identification of mixtures satisfying our four physical constraints.

4. Discussions

4.1. Training of ANNs

Concerning the hyperparameters, the most efficient ones depend on the test. The selu activation function performs better for the prediction

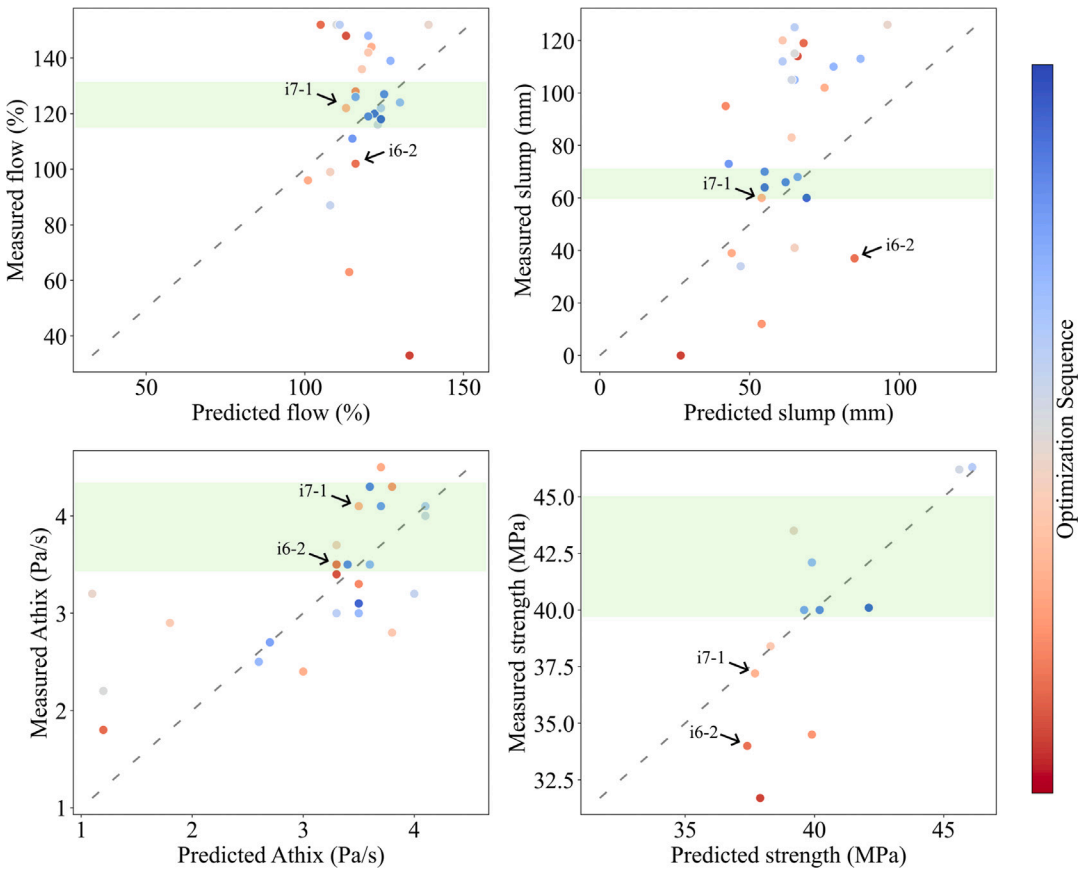

Fig. 7. All measured vs predicted results for iterations 1 to 9: the colors (red to green) represent the advancement of the iterations for a given search space and set of objectives, the green areas represent the physical objectives for printability (Table 4). In the bottom right graph, the green area depicts the 40 MPa strength objective set for the iterations i6 to i9. (For interpretation of the references to color in this figure legend, the reader is referred to the web version of this article.)

Table 10
Iteration average relative errors in % of 3 mixtures compared to ANN predictions (pred) and printability objectives (obj) for flow, slump, Athix and compressive strength. Average-pred and Average-obj are the average errors of all tests for each iteration.

Iteration	Flow-pred	Slump-pred	Athix-pred	Strength-pred	Average-pred	Flow-obj	Slump-obj	Athix-obj	Strength-obj	Average-obj
i1	20	79	10	7	36	0	59	13		24
i2	30	66	53	27	50	0	66	23		30
i3	10	49	7	15	22	3	25	10		12
i4	19	40	29	43	29	13	53	16		27
i5	10	25	15	25	16	9	39	4		17
i6	44	78	40	13	44	45	75	0	17	34
i7	12	47	78	4	35	0	59	10	4	18
i8	4	59	6	2	18	1	69	5	0	19
i9	5	14	5	2	7	1	0	11	0	3

of flow and slump results whereas the tanh and softsign are alternatively the best choices for the Athix. The optimal number of layers is generally between 4 and 5 and the learning rate varies significantly in the defined boundaries. In the end, the mean coefficients of determination for ANNs on all data are respectively 0.93, 0.88, and 0.76 for flow, slump, and Athix. From the sixth iteration, when the compressive strength was included, the mean coefficient of determination of all data for predicted compressive strength is 0.75.

4.2. Reduction of workload

This methodology allows the satisfactory predictions of three rheological properties for a 6-parameter mixture in a local design space. For a design of experiments with 6 factors and 3 levels, the use of a full factorial design or a fractional factorial design would respectively lead to 729 and 243 mixtures. This methodology allows us to get reliable tendencies and printable results in 36 to 54 mixtures for two different applications. This process is all the more relevant in this 3D printing application as the decoupling between high flow and low slump results can lead to a counter-intuitive trial-and-error design. When including also the structuration rate and the compressive strength, the suggested mixtures proposed by this tool significantly decrease the design complexity.

The global process does not aim to establish generalized predictive models for material properties, but more so to rapidly orient the suggested mixtures toward a locally prediction-accurate design space, making it easier to find suitable 3D printing materials.

4.3. Minimization of climate change score for identified mixtures

For iterations 1 to 5, the optimality is defined as the minimization of the ClCh score and the satisfaction of printability criteria in the design space boundaries. The presented results alone do not demonstrate the optimality for the mixtures i3-3 (236 kg CO_2-eq/m^3 and i5-3 (226 kg

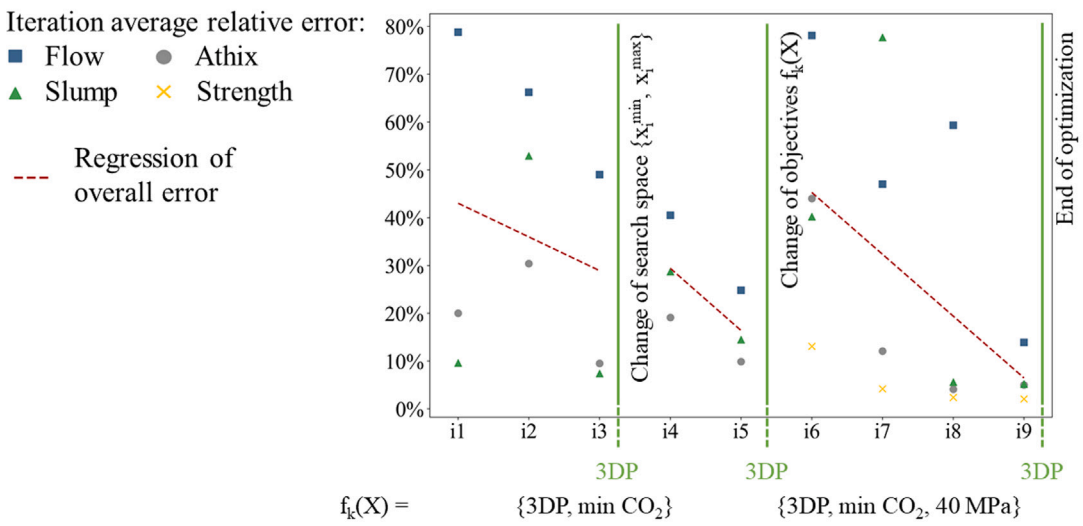

Fig. 8. Iteration average relative errors of ANN predictions: points represent the average error of 3 suggested mixtures for experimental tests, red dash lines are the linear regressions of average errors across all tests, the divisions in green depict the changes in search space and the change in objectives.

CO_2-eq/m^3) as the minimal ClCh scores corresponding to the parameter boundaries in the first optimization (without strength) are respectively 214 and 186 kg CO_2-eq/m^3. Of course, the mixtures corresponding to these minima are not printable. Moreover, all the experimental data indicate that a minimum of 120 kg/m^3 (average value of 133 kg/m^3) of CC is necessary to simultaneously attain 110% flow and 3.5 Pa/s Athix. With this consideration, the minimal ClCh scores for the parameter boundaries in Table 6 are respectively 221 and 206 kg CO_2-eq/m^3. In the end, the results of this sequence can be considered close to local optima for these boundaries, taking into account constraints of sand/paste ratio for adequate workability.

Concerning the mixture i9-2 (printable, 40 MPa), several considerations lead to the affirmation of its optimality. The Athix and strength of i9-2 are respectively 3.5 Pa/s and 40 MPa, which just satisfy the constraints, meaning it would be challenging to reduce the GUbSF and calcined clay volumes without a sharp decrease in W/binder ratio. However, the iteration i8 showed difficulty in attaining flow and slump decoupling with lower W/binder (and liquid/solid) ratios. Furthermore, the mixture i9-1, which presents a higher SP proportion than i9-2 (0.34 vs 0.31 wt%) exhibits poor Athix (2.7 Pa/s). Consequently, as the GUbSF and CC contents are the main drivers of the ClCh score, the latter is considered to be minimized in this range of compressive strength.

Another approach, not carried out in this study, would have been to determine an optimum around the reference mixture (Table 2), while keeping a 30 MPa criterion for compressive strength.

4.4. Relationships between mortar constituents and physical properties

In this section, we identify the main factors influencing the response variables. The Fig. 9 depicts the effects of different parameters (cement content, CC/binder, LF/binder, W/binder, Sa/paste, SP/binder) on the flow, slump, Athix and strength. The binder is composed of GUbSF (cement with silica fume), CC (calcined clay) and LF (limestone filler). The paste includes the binder, the water and the superplasticizer. The red line represents the linear regression of all the collected data and the red area around the line depicts the 95% confidence interval. In addition to that, the green colored graphs are the statistically significant interactions.

To identify the meaningful contributions, an ANOVA is carried out with a simple multi-linear regression model, such as the effect of an independent variable on a response variable is statistically significant for a p-value < 0.05. With these considerations, the flow and slump are impacted mainly by the W/binder and SP/binder ratios. On the other hand, the Athix is heavily influenced by the W/binder ratio and the CC/binder ratio. To a lesser extent, the Sa/paste ratio contributes to the Athix value. For the strength, the GUbSF content is the most significant parameter, as expected. The W/binder ratio also has a meaningful impact on strength. the LF/binder and Sa/paste contributions are statistically significant as they influence respectively the cement content and the paste volume.

In the context of this study, no mortar constituent is fixed, which broadens the design space for determining optima. That means every mixture's physical response is influenced by every parameter simultaneously. As such, concurrent evaluation of flow, slump and Athix values may be counter-intuitive. For example, if we consider the variations of W/CC and CC volume from mixture DoE-1 to DoE-2 and DoE-7 to DoE-8 from the Table 5, they are both follow the same trend but lead to respectively an increase and decrease of Athix. This counter-intuitive result is explained by the higher W/CC ratio of mixture 8. These mixtures are simply in different design spaces where variations in entry parameters can lead to different responses. Another example is the mixture 10, which follows a different trend for which the Athix does not decrease when the flow and slump increase. Compared to mixture 3 which has similar W/CC ratio and slightly higher CC content, the Athix remains similar. Still, for these mixtures, flow and slump are not in the same range, meaning other non-fixed parameters influence the Athix results.

In a similar fashion, results of flow and slump according to SP proportions may be unexpected. For instance, the mixture i5-1 displays a low slump (34 mm) despite a high SP proportion (0.37 wt%). However, the liquid/solid (L/S) ratio is among the lowest for all mixtures. It is known that the effect of water content on workability is non-linear. Above a certain threshold of L/S ratio (and binder volume), the paste sufficiently coats the aggregates, rendering a hydrodynamic flow regime, as compared to frictional granular regime. If we look at other slump values with low L/S ratios (mixtures i8-1, i8-2, i8-3), they

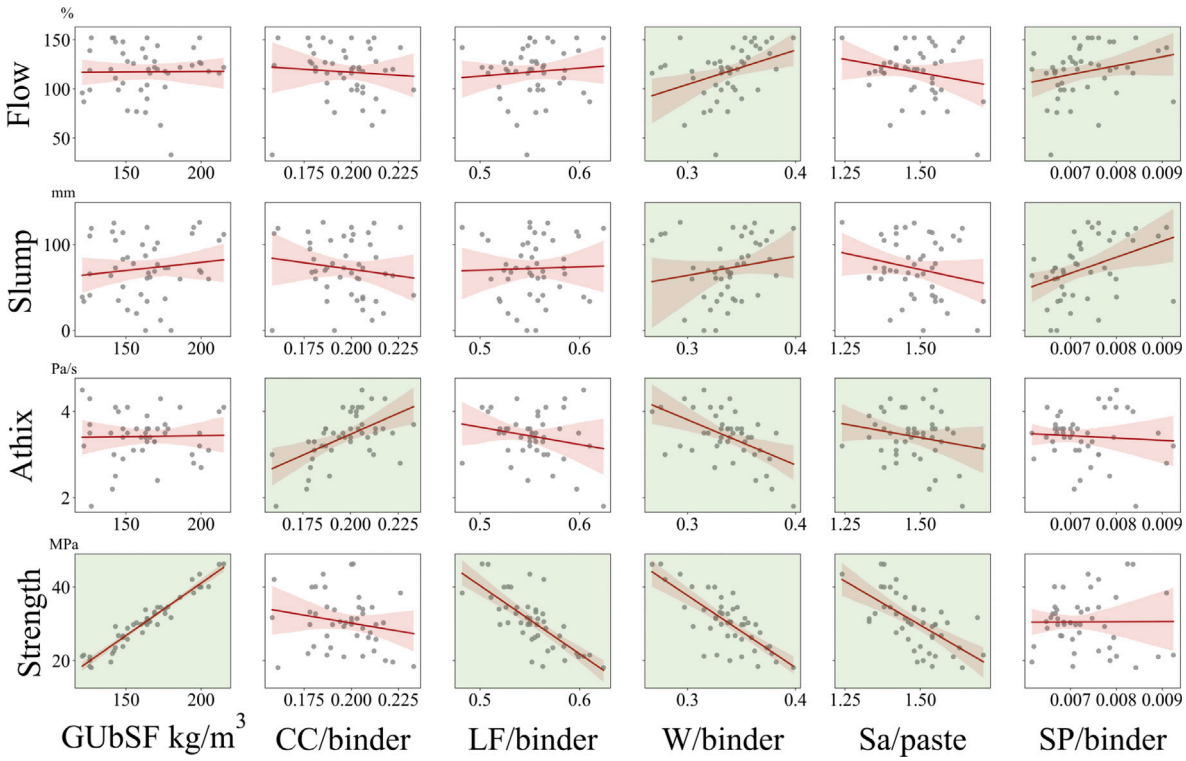

Fig. 9. Effects of cement content (kg/m^3) as well as CC/binder, LF/binder, W/binder, Sa/paste and SP/binder ratios on flow (%), slump (mm), Athix (Pa/s) and strength (MPa) for all collected data: Red line are the linear regressions for each plot, displayed with a 95% confidence interval (red area). Highlighted green plots represent meaningful contributions (p-value < 0.05). (For interpretation of the references to color in this figure legend, the reader is referred to the web version of this article.)

are higher than i5-1 (respectively 116,122, 124 mm). This is explained by the much higher paste volume (≈ 258 vs 218 cm^3) design region explored in the iteration 8. These examples highlight the difficulties in analyzing highly complex interactions, justifying the application of this data-driven optimization methodology.

4.5. Specific role of calcined clay in low-clinker LC3-based materials

The structuration rates attained in this study confirm the potential LC3-based materials hold for one-component 3D printing. This section details the specific impact of calcined clay on the physical properties of the formed mixtures, as CC is the differentiating factor of LC3. The Fig. 10 shows all the experimental results of Athix with respect to water/calcined clay ratio (W/CC) (left) and calcined clay volume (right). The CC content seems to influence the Athix value, but the latter is more dependent on the W/binder ratio, and more specifically with the W/CC ratio.

Counter-intuitively, the CC proportion is not a determining factor for the compressive strength (R^2 = 0.34), especially compared to GUbSF volume (R^2 = 0.94). This can be attributed to the low clinker proportion, which entails an insufficient portlandite availability [64], preventing the formation of all potential C-(A)-S-H hydration products. As a result, we observe a distinct influence of cement content on the strength provided by calcined clay hydration. The Fig. 11 depicts the compressive strength (MPa) delivered by unit volume of CC according to the GUbSF content. It demonstrates that the contribution of calcined clay to compressive strength is dependent on the clinker content. Also, it is observed that the reduction of alite hydration in an undersulfated system, such as our low-clinker blends, hinders strength development, especially for increased aluminum concentrations [65]. A sulfate adjustment with the addition of gypsum is beneficial for the setting rate and final strength but prevents the flash structuration desired for continuous mixing 3D printing. This additional parameter could be added to the optimization process to quickly obtain a proper sulfate balance with respect to a desired structuration rate.

4.6. Limitations

In this study, the mixtures formed are selected by the user at each iteration. These solutions must represent the largest region presenting potential optimal mixtures. As the process advances, the selection of solutions is driven toward the optimal design region. Although the selection of Pareto-optimal solutions to form is still a user input, which requires an evaluation of their quality, the choice of formulations to assess is made considerably easier than progressing through trial-and-error. This could be improved by using the Technique for Order of Preference by Similarity to Ideal Solution (TOPSIS) [66] or attributing weights and automatically selecting the best overall solution along with two solutions that perform best in two distinct objectives.

On Fig. 8, the average errors between predictions and measurements are substantial. The choice made in this paper was to end a round of optimization in a definite search space whenever a mixture satisfied all objectives set beforehand. If the first optimization sequence (Section 3.2) had been prolonged, we believe the overall error on Fig. 8 would have decreased below 10% as it did for the iteration i9. As mentioned above, the global objective is not to propose a predictive tool, but rather an optimum-driven strategy for the mixture design of complex materials with more than 3 independent variables and several output objectives.

Concerning the choice of machine learning algorithms, neural networks have been dominant in concrete science since 1992 and used for most classification tasks [26,35] but random forest algorithms could be more accurate on discrete data [31]. In terms of stochastic algorithms for complex multiobjective problems, the difference mainly resides in the selection operators. The *NSGA-II* remains the most popular choice [41] but other meta-heuristics (*multiobjective Particle Swarm Optimization, Strength Pareto Evolutionary Algorithm, Pareto Archived Evolution Strategy*) could be tested to see if it facilitates the sometimes difficult selection of quality suggested mixtures.

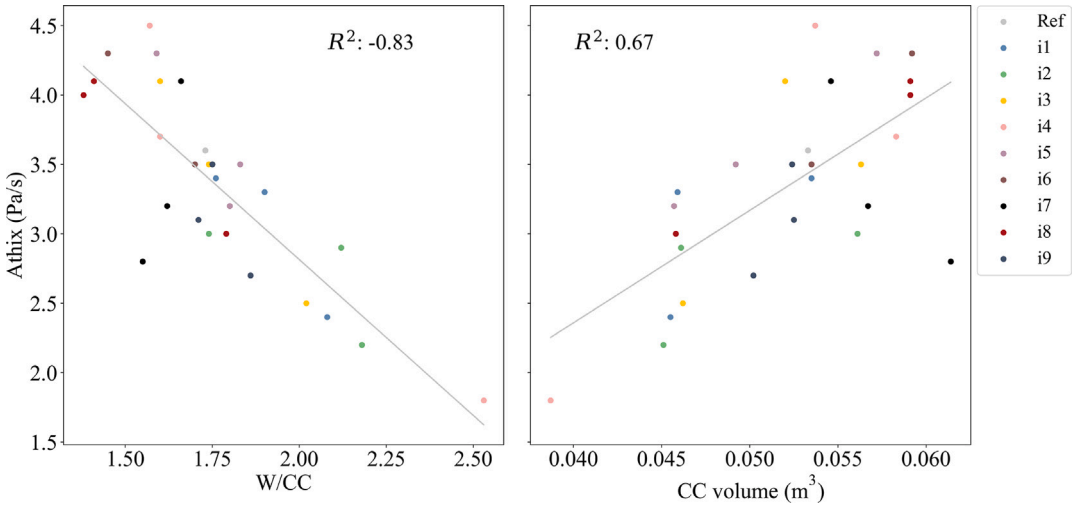

Fig. 10. Athix values versus water/calcined clay ratio (left) and calcined clay volume (right) for the reference material (Ref) and all iterations.

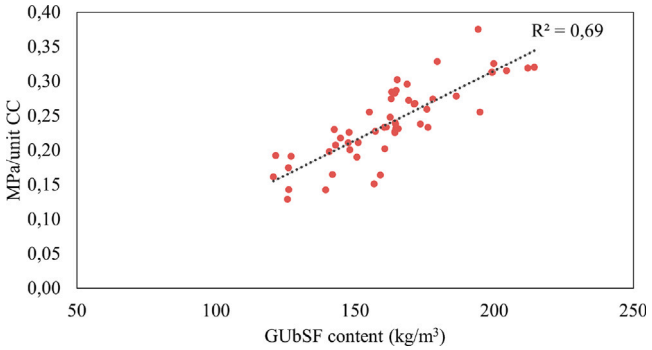

Fig. 11. Strength (MPa) provided by calcined clay hydration based on GUbSF content.

5. Conclusion

As new, more sophisticated construction techniques emerge, concrete design becomes more elaborate. With imperatives of rheological suitability and mechanical performance, studies using traditional mixture design methods tend to overlook the environmental impacts. The present study highlights the efficiency of combining stochastic multi-objective optimization with life cycle assessment and artificial neural networks for minimizing the environmental impact of 3D printable quaternary LC3-based composites. Compared to traditional mixture design methods, the present technique allows quick convergence toward a relevant design region, thus yielding appropriate mixtures in 3 to 5 experimental iterations (9 to 15 mixtures). Considering the high number of independent variables and conflicting objective functions, we believe this mixture design strategy to considerably reduce the workload and resource use. Overall, we propose a reproducible mixture design methodology adapted to locally sourced materials. Furthermore, its flexibility enables the use of different characterization procedures applied to the majority of 3D printing materials.

The reference mixture with 6.8 wt% cement, 251 kg CO_2-eq/m^3, 30 MPa required 22 trial-and-error mixtures with fixed mortar constituents and arbitrary performance-based progression. Conversely, mixtures with 5.3 wt% cement, 226 kg CO_2-eq/m^3, 20 MPa and 8.3 wt% cement, 280 kg CO_2-eq/m^3, 40 MPa (respectively i5-3 and i9-2) were determined via our optimum-driven approach. These mixtures are close to optima and constitute eco-efficient solutions for continuous one-component 3D printing compared to the literature.

In a further study, physics-informed neural networks [35,67] could enhance the accuracy of predictions and allow faster convergence, especially if investigating unexplored search spaces with limited data. For instance, the presented methodology could be applied to high-performance LC3, which should prove to be greatly eco-efficient (low kg CO_2-eq.m^{-3}/MPa) for high-performance applications. Experiments on durability are also needed to determine the exposition class and suitable applications.

CRediT authorship contribution statement

Willy Jin: Writing – original draft, Software, Methodology, Investigation, Data curation, Conceptualization. **Jean-François Caron:** Writing – review & editing, Supervision, Resources, Funding acquisition, Conceptualization. **Claudiane M. Ouellet-Plamondon:** Writing – review & editing, Resources, Methodology, Funding acquisition, Conceptualization.

Declaration of competing interest

The authors declare that they have no known competing financial interests or personal relationships that could have appeared to influence the work reported in this paper.

Acknowledgments

The authors would like to thank the Canada Research Chair program (CRC-2019-00074), the Canadian Foundation for Innovation (CFI/FCI #37692) and the LABEX MMCD for funding this research.

Data availability

Data will be made available on request.

References

[1] Z. Zhao, C. Ji, J. Xiao, L. Yao, C. Lin, T. Ding, T. Ye, A critical review on reducing the environmental impact of 3D printing concrete: Material preparation, construction process and structure level, Constr. Build. Mater. 409 (2023) 133887.
[2] C. Zhang, V.N. Nerella, A. Krishna, S. Wang, Y. Zhang, V. Mechtcherine, N. Banthia, Mix design concepts for 3D printable concrete: A review, Cem. Concr. Compos. 122 (2021) 104155.
[3] Y. Chen, F. Veer, O. Çopuro, A critical review of 3D concrete printing as a low CO2 concrete approach, Heron 62 (2017) 167–194.
[4] H. Alhumayani, M. Gomaa, V. Soebarto, W. Jabi, Environmental assessment of large-scale 3D printing in construction: A comparative study between cob and concrete, J. Clean. Prod. 270 (2020) 122463.

[5] N. Roussel, A thixotropy model for fresh fluid concretes: Theory, validation and applications, Cem. Concr. Res. 36 (10) (2006) 1797–1806.
[6] N. Roussel, Rheological requirements for printable concretes, Cem. Concr. Res. 112 (2018) 76–85.
[7] K. Kuzmenko, N. Gaudillière-Jami, A.d. Feraille, J. Dirrenberger, O. Baverel, Assessing the Environmental Viability of 3D Concrete Printing Technology, in: Design Modelling Symposium Berlin, Springer, Cham, 2020, pp. 517–528.
[8] K.L. Scrivener, V.M. John, E.M. Gartner, Eco-efficient cements: Potential economically viable solutions for a low-CO2 cement-based materials industry, Cem. Concr. Res. 114 (2018) 2–26.
[9] K. Scrivener, F. Martirena, S. Bishnoi, S. Maity, Calcined clay limestone cements (LC3), Cem. Concr. Res. 114 (2018) 49–56.
[10] M. Antoni, J. Rossen, F. Martirena, K. Scrivener, Cement substitution by a combination of metakaolin and limestone, Cem. Concr. Res. 42 (12) (2012) 1579–1589.
[11] M. Sharma, S. Bishnoi, F. Martirena, K. Scrivener, Limestone calcined clay cement and concrete: A state-of-the-art review, Cem. Concr. Res. 149 (2021) 106564.
[12] F. Zunino, K. Scrivener, Insights on the role of alumina content and the filler effect on the sulfate requirement of PC and blended cements, Cem. Concr. Res. 160 (2022) 106929.
[13] F. Zunino, K. Scrivener, The reaction between metakaolin and limestone and its effect in porosity refinement and mechanical properties, Cem. Concr. Res. 140 (2021) 106307.
[14] F. Zunino, K. Scrivener, Microstructural developments of limestone calcined clay cement (LC3) pastes after long-term (3 years) hydration, Cem. Concr. Res. 153 (2022) 106693.
[15] Y. Chen, S. He, Y. Zhang, Z. Wan, O. Çopuroğlu, E. Schlangen, 3D printing of calcined clay-limestone-based cementitious materials, Cem. Concr. Res. 149 (2021) 106553.
[16] W.-J. Long, C. Lin, J.-L. Tao, T.-H. Ye, Y. Fang, Printability and particle packing of 3D-printable limestone calcined clay cement composites, Constr. Build. Mater. 282 (2021) 122647.
[17] S. Bhattacherjee, S. Jain, M. Santhanam, Developing 3D printable and buildable limestone calcined clay-based cement composites with higher aggregate content, Constr. Build. Mater. 376 (2023) 131058.
[18] T.R. Muzenda, P. Hou, S. Kawashima, T. Sui, X. Cheng, The role of limestone and calcined clay on the rheological properties of LC3, Cem. Concr. Compos. 107 (2020) 103516.
[19] M. Beigh, V.N. Nerella, E. Secrieru, V. Mechtcherine, Structural build-up behavior of limestone calcined clay cement (LC^3) pastes in the context of digital concrete construction, in: 2nd International Conference on Rheology and Processing of Construction Materials (RheoCon2), Rheology and Processing of Construction Materials, 2019.
[20] P. Hou, T.R. Muzenda, Q. Li, H. Chen, S. Kawashima, T. Sui, H. Yong, N. Xie, X. Cheng, Mechanisms dominating thixotropy in limestone calcined clay cement (LC3), Cem. Concr. Res. 140 (2021) 106316.
[21] K. Vance, A. Kumar, G. Sant, N. Neithalath, The rheological properties of ternary binders containing Portland cement, limestone, and metakaolin or fly ash, Cem. Concr. Res. 52 (2013) 196–207.
[22] P. Tennis, M. Thomas, W. Weiss, State-of-the-Art Report on Use of Limestone in Cements at Levels of up to 15%, 2011, PCA R&D SN3148.
[23] S. Bhattacherjee, A.S. Basavaraj, A. Rahul, M. Santhanam, R. Gettu, B. Panda, E. Schlangen, Y. Chen, O. Copuroglu, G. Ma, L. Wang, M.A. Basit Beigh, V. Mechtcherine, Sustainable materials for 3D concrete printing, Cem. Concr. Compos. 122 (2021) 104156.
[24] G. Bai, L. Wang, G. Ma, J. Sanjayan, M. Bai, 3D printing eco-friendly concrete containing under-utilised and waste solids as aggregates, Cem. Concr. Compos. 120 (2021) 104037.
[25] S. Kosmatka, M. Wilson, Design and Control of Concrete Mixtures, fourtenth ed., Portland Cement Association, 2011.
[26] M.A. DeRousseau, J.R. Kasprzyk, W.V. Srubar, Computational design optimization of concrete mixtures: A review, Cem. Concr. Res. 109 (2018) 42–53.
[27] Z. Liu, M. Li, Y. Weng, T.N. Wong, M.J. Tan, Mixture Design Approach to optimize the rheological properties of the material used in 3D cementitious material printing, Constr. Build. Mater. 198 (2019) 245–255.
[28] S. Chidiac, F. Moutassem, F. Mahmoodzadeh, Compressive strength model for concrete, Mag. Concr. Res. 65 (2013) 557–572.
[29] V. De Bono, N. Ducoulombier, R. Mesnil, J.F. Caron, Methodology for formulating low-carbon printable mortar through particles packing optimization, Cem. Concr. Res. 176 (2024) 107403.
[30] S.E. Chidiac, F. Mahmoodzadeh, Plastic viscosity of fresh concrete – a critical review of predictions methods, Cem. Concr. Compos. 31 (8) (2009) 535–544.
[31] J. Zhang, Y. Huang, Y. Wang, G. Ma, Multi-objective optimization of concrete mixture proportions using machine learning and metaheuristic algorithms, Constr. Build. Mater. 253 (2020) 119208.
[32] V. Shobeiri, B. Bennett, T. Xie, P. Visintin, A generic framework for augmented concrete mix design: Optimisation of geopolymer concrete considering environmental, financial and mechanical properties, J. Clean. Prod. 369 (2022) 133382.
[33] A. Öztaş, M. Pala, E.a. Özbay, E.a. Kanca, N. Çağˇ lar, M.A. Bhatti, Predicting the compressive strength and slump of high strength concrete using neural network, Constr. Build. Mater. 20 (9) (2006) 769–775.
[34] M.M. Alshihri, A.M. Azmy, M.S. El-Bisy, Neural networks for predicting compressive strength of structural light weight concrete, Constr. Build. Mater. 23 (6) (2009) 2214–2219.
[35] Z. Li, J. Yoon, R. Zhang, F. Rajabipour, W.V. Srubar III, I. Dabo, A. Radlińska, Machine learning in concrete science: applications, challenges, and best practices, npj Comput. Mater. 8 (1) (2022) 1–17, Publisher: Nature Publishing Group.
[36] V. Sergis, C.M. Ouellet-Plamondon, Automating mix design for 3D concrete printing using optimization methods, Dig. Discover. (2022).
[37] M.A. DeRousseau, J.R. Kasprzyk, W.V.I. Srubar, Multi-objective optimization methods for designing low-carbon concrete mixtures, Front. Mater. 8 (2021) Publisher: Frontiers.
[38] S.-Y. Geng, Q.-L. Luo, B.-Y. Cheng, L.-X. Li, D.-C. Wen, W.-J. Long, Intelligent multi-objective optimization of 3D printing low-carbon concrete for multi-scenario requirements, J. Clean. Prod. 445 (2024) 141361.
[39] A. López Jaimes, S. Zapotecas-Martínez, C. Coello, An introduction to multiobjective optimization techniques, in: Optimization in Polymer Processing, Nova Science Publishers, 2011, pp. 29–57.
[40] K. Deb, A. Pratap, S. Agarwal, T. Meyarivan, A fast and elitist multiobjective genetic algorithm: NSGA-II, IEEE Trans. Evol. Comput. 6 (2) (2002) 182–197, Conference Name: IEEE Transactions on Evolutionary Computation.
[41] J.L.J. Pereira, G.A. Oliver, M.B. Francisco, S.S. Cunha, G.F. Gomes, A review of multi-objective optimization: Methods and algorithms in mechanical engineering problems, Arch. Comput. Methods Eng. 29 (4) (2022) 2285–2308.
[42] W. Jin, C. Roux, C. Ouellet-Plamondon, J.-F. Caron, Life cycle assessment of limestone calcined clay concrete: Potential for low-carbon 3D printing, Sustain. Mater. Technol. 41 (2024) e01119.
[43] C. Mutel, Brightway: An open source framework for Life Cycle Assessment, J. Open Source Softw. 2 (12) (2017) 236.
[44] Joint Research Centre (European Commission), E.M. Schau, V. Castellani, S. Fazio, E. Diaconu, S. Sala, L. Zampori, M. Secchi, Supporting information to the characterisation factors of recommended E Life Cycle Impact Assessment methods: new methods and differences with ILCD, Publications Office of the European Union, LU, 2018.
[45] ASTM, C1437, Standard test method for flow of hydraulic cement mortar, 2007, C1437.
[46] C. ASTM, 143/C143M: Standard test method for slump of hydraulic-cement concrete, Annual Book of ASTM Standards, vol. 4, 2010, pp. 89–91.
[47] N. Roussel, P. Coussot, "Fifty-cent rheometer" for yield stress measurements: From slump to spreading flow, J. Rheol. 49 (3) (2005) 705–718, Publisher: The Society of Rheology.
[48] D. ASTM, Standard test method for direct shear test of soils under consolidated drained conditions, 2011, p. 9, D3080/D3080M, vol. 3.
[49] V. Sergis, C. Ouellet-Plamondon, D-optimal design of experiments applied to 3D high-performance concrete printing mix design, Mater. Des. (2022) 110681.
[50] R. Wolfs, F. Bos, T. Salet, Early age mechanical behaviour of 3D printed concrete: Numerical modelling and experimental testing, Cem. Concr. Res. 106 (2018) 103–116.
[51] ASTM, Standard test method for compressive strength of hydraulic cement mortars (using 2-in. or [50-mm] cube specimens), ASTM International, 2013.
[52] S. Cho, J. Kruger, F. Bester, M. van den Heever, A. van Rooyen, G. van Zijl, A compendious Rheo-mechanical test for printability Assessment of 3D printable concrete, in: F.P. Bos, S.S. Lucas, R.J. Wolfs, T.A. Salet (Eds.), Second RILEM International Conference on Concrete and Digital Fabrication, Springer International Publishing, Cham, 2020, pp. 196–205.
[53] Y.W.D. Tay, Y. Qian, M.J. Tan, Printability region for 3D concrete printing using slump and slump flow test, Composites B 174 (2019) 106968.
[54] G. Ma, Z. Li, L. Wang, Printable properties of cementitious material containing copper tailings for extrusion based 3D printing, Constr. Build. Mater. 162 (2018) 613–627.
[55] M.K. Mohan, A.V. Rahul, K. Van Tittelboom, G. De Schutter, Rheological and pumping behaviour of 3D printable cementitious materials with varying aggregate content, Cem. Concr. Res. 139 (2021) 106258.
[56] V. Nerella, M. Näther, A. Iqbal, M. Butler, V. Mechtcherine, Inline quantification of extrudability of cementitious materials for digital construction, Cem. Concr. Compos. 95 (2019) 260–270.
[57] S. Muthukrishnan, H.W. Kua, L.N. Yu, J.K.H. Chung, Fresh properties of cementitious materials containing rice husk ash for construction 3D printing, J. Mater. Civ. Eng. 32 (8) (2020) 04020195, Publisher: American Society of Civil Engineers.
[58] M.A. Khan, Mix suitable for concrete 3D printing: A review, Mater. Today: Proc. 32 (2020) 831–837.
[59] Y. Chen, C. Romero Rodriguez, Z. Li, B. Chen, O. Çopuroğlu, E. Schlangen, Effect of different grade levels of calcined clays on fresh and hardened properties of ternary-blended cementitious materials for 3D printing, Cem. Concr. Compos. 114 (2020) 103708.

[60] C. Liu, X. Wang, Y. Chen, C. Zhang, L. Ma, Z. Deng, C. Chen, Y. Zhang, J. Pan, N. Banthia, Influence of hydroxypropyl methylcellulose and silica fume on stability, rheological properties, and printability of 3D printing foam concrete, Cem. Concr. Compos. 122 (2021) 104158.

[61] V. Sergis, Hyperautomation of 3D Concrete Printing by Introducing Artificial Intelligence (Ph.D. thesis), École de Technologie Supérieure, Université du Québec, Montréal, 2023.

[62] P. Goos, B. Jones, Optimal design of experiments: a case study approach, EMWYkYd3sPoC, John Wiley & Sons, 2011, Google-Books-ID.

[63] J. Yammine, M. Chaouche, M. Guerinet, M. Moranville, N. Roussel, From ordinary rhelogy concrete to self compacting concrete: A transition between frictional and hydrodynamic interactions, Cem. Concr. Res. 38 (7) (2008) 890–896.

[64] S. Krishnan, D. Gopala Rao, S. Bishnoi, Why low-grade calcined clays are the ideal for the production of limestone calcined clay cement (LC3), in: S. Bishnoi (Ed.), Calcined Clays for Sustainable Concrete, in: RILEM Bookseries, Springer, Singapore, 2020, pp. 125–130.

[65] M. Maier, R. Sposito, N. Beuntner, K.-C. Thienel, Particle characteristics of calcined clays and limestone and their impact on early hydration and sulfate demand of blended cement, Cem. Concr. Res. 154 (2022) 106736.

[66] R. Vavrek, Evaluation of the impact of selected weighting methods on the results of the TOPSIS technique, Int. J. Inf. Technol. Decis. Mak. 18 (06) (2019) 1821–1843, Publisher: World Scientific Publishing Co..

[67] J. Willard, X. Jia, S. Xu, M. Steinbach, V. Kumar, Integrating scientific knowledge with machine learning for engineering and environmental systems, ACM Comput. Surv. 55 (4) (2022) 66:1–66:37.